





Controlled phage therapy by photothermal ablation of specific bacterial species using gold nanorods targeted by chimeric phages

Huan Peng^a, Raymond E. Borg^a, Liam P. Dow^b, Beth L. Pruitt^{b,c,d} , and Irene A. Chen^{a,b,e,1} 

^aDepartment of Chemistry and Biochemistry, University of California, Santa Barbara, CA 93106; ^bProgram in Biomolecular Science and Engineering, University of California, Santa Barbara, CA 93106; ^cDepartment of Mechanical Engineering, University of California, Santa Barbara, CA 93106; ^dDepartment of Molecular, Cellular, and Developmental Biology, University of California, Santa Barbara, CA 93106; and ^eDepartment of Chemical and Biomolecular Engineering, University of California, Los Angeles, CA 90095

Edited by Catherine J. Murphy, University of Illinois at Urbana–Champaign, Urbana, IL, and approved December 12, 2019 (received for review August 1, 2019)

The use of bacteriophages (phages) for antibacterial therapy is under increasing consideration to treat antimicrobial-resistant infections. Phages have evolved multiple mechanisms to target their bacterial hosts, such as high-affinity, environmentally hardy receptor-binding proteins. However, traditional phage therapy suffers from multiple challenges stemming from the use of an exponentially replicating, evolving entity whose biology is not fully characterized (e.g., potential gene transduction). To address this problem, we conjugate the phages to gold nanorods, creating a reagent that can be destroyed upon use (termed “phanorods”). Chimeric phages were engineered to attach specifically to several Gram-negative organisms, including the human pathogens *Escherichia coli*, *Pseudomonas aeruginosa*, and *Vibrio cholerae*, and the plant pathogen *Xanthomonas campestris*. The bioconjugated phanorods could selectively target and kill specific bacterial cells using photothermal ablation. Following excitation by near-infrared light, gold nanorods release energy through nonradiative decay pathways, locally generating heat that efficiently kills targeted bacterial cells. Specificity was highlighted in the context of a *P. aeruginosa* biofilm, in which phanorod irradiation killed bacterial cells while causing minimal damage to epithelial cells. Local temperature and viscosity measurements revealed highly localized and selective ablation of the bacteria. Irradiation of the phanorods also destroyed the phages, preventing replication and reducing potential risks of traditional phage therapy while enabling control over dosing. The phanorod strategy integrates the highly evolved targeting strategies of phages with the photothermal properties of gold nanorods, creating a well-controlled platform for systematic killing of bacterial cells.

bacteriophage | phage therapy | gold nanorods

Antibiotic-resistant bacterial infections, particularly from Gram-negative organisms, are widely recognized as an urgent threat to health worldwide (1). The development of new antibacterial agents targeting these organisms is therefore an important goal. Phages have been long proposed as antibacterial agents, and recent case studies (2, 3) and clinical trials (4) have prompted increased attention. However, treatment of infection by whole phages presents critical challenges, such as a lack of biological characterization of most phages, which may carry toxin genes or cause generalized transduction of bacterial genes (5). An interesting approach uses phages to deliver CRISPR-Cas cassettes as antimicrobials (6, 7), although this strategy faces challenges with efficient delivery to a wider range of bacterial targets (8). In addition, the pharmacokinetics and pharmacodynamics of phages are difficult to model due to their exponential replication, presenting a major barrier to clinical translation (9). Exponential replication may also lead to undesirably rapid release of bacterial endotoxins (10). A reductionist approach to avoid the problems associated with whole phages is to engineer phage-derived proteins, such as pyocins or lysins, as antibacterial agents (reviewed in ref. 11). However, some advantages of whole phages, such as avidity of the

phage-displayed receptor-binding proteins (RBPs), which may increase affinity by ~1,000× compared to recombinant RBP (12), interaction with secondary receptors on the bacterial host (13, 14), and subdiffusive search mechanisms (15, 16), may be lost. Therefore, an alternative approach is to utilize the phage for bacterial attachment, and then destroy the phages simultaneously with the bacteria, thus controlling dosage and avoiding undesired consequences while maintaining the advantages of whole phage as a delivery vehicle.

Here, we use photothermal heating as a physical mechanism that would result in both phage and host cell destruction, which can be achieved using metallic nanomaterials (17–22). These nanostructures, such as gold nanorods (AuNRs), exhibit a localized surface plasmon resonance (LSPR) upon irradiation with light, which induces coherent oscillation of the electron cloud. This energy can be released primarily as heat, leading to high local temperatures (e.g., ΔT up to ~50 °C, depending on the laser power applied) with a half-length in the submicron range (from a single nanoparticle) to a few microns (from an ensemble of nanoparticles) (23, 24), potentially killing nearby bacterial or eukaryotic cells. The LSPR spectrum of AuNRs can be tuned by their size, allowing excitation by light in the near-infrared (NIR)

Significance

New methods for detecting and killing antibiotic-resistant, Gram-negative bacteria are of prime interest for a wide variety of applications. While phages have long been considered as potential antibacterial agents, many concerns about phage therapy stem from the fact that phages are replicating, evolvable entities whose biology is poorly understood in most cases. These concerns could be addressed by destroying the phage immediately upon use. We accomplish this by conjugating phages to gold nanorods, whose excitation by near-infrared light causes localized heating that essentially cooks nearby bacteria. Thus, the phages deliver gold nanorods to the targeted bacteria, and the nanorods destroy both bacteria and phages simultaneously. This strategy transforms phages from an evolving biological entity into a controlled, drug-like reagent.

Author contributions: H.P. and I.A.C. designed research; H.P. and R.E.B. performed research; H.P., L.P.D., and B.L.P. contributed new reagents/analytic tools; H.P. and I.A.C. analyzed data; and H.P. and I.A.C. wrote the paper.

Competing interest statement: A provisional patent application has been filed: University of California, Santa Barbara case 2018-758.

This article is a PNAS Direct Submission.

This open access article is distributed under Creative Commons Attribution-NonCommercial-NoDerivatives License 4.0 (CC BY-NC-ND).

¹To whom correspondence may be addressed. Email: chen@chem.ucsb.edu.

This article contains supporting information online at <https://www.pnas.org/lookup/suppl/doi:10.1073/pnas.1913234117/-DCSupplemental>.

First published January 13, 2020.

“biological window” for which soft tissues are somewhat transparent. Other nanomaterials also exhibit nonspecific cytotoxic properties (e.g., nanosilver) through a variety of chemical mechanisms, but a general problem with the application of nanomaterials against bacterial infections is their lack of specificity against bacterial vs. mammalian cells, presenting a general challenge for biocompatibility (25).

To confer specificity to nanostructures, one may conjugate antibodies that target specific bacterial strains (26), following upon extensive work targeting nanoparticles for cancer cell treatment (27–30). However, phage-based strategies possess several advantages compared to antibody-based strategies. First, greater delivery of nanoparticles per bacterial receptor could be achieved using phages due to the comparatively large surface area of phage, which may accommodate multiple nanoparticles; this property could be useful if bacterial receptors are in low abundance. A related benefit is that the aggregation of nanoparticles with phages on bacteria produces a visible shift in the LSPR spectrum (31), and one might therefore envision applications that combine treatment and detection of bacteria. Second, in addition to the targeting mechanisms evolved by whole phages as described above, chimeric phages can be rationally designed to achieve specificity against different bacterial hosts (8). This potential is largely untapped, as there exists a mostly uncharacterized biological reservoir of phages that could presumably target many different bacterial strains (32). While phages are well known for their host specificity, a number are broad in host range (33), suggesting that the degree of specificity could be tuned depending on the desired application. Third, in practical terms, phages are inexpensive to produce and have typically evolved some hardiness to nonideal environmental conditions. These features make phage-based nanotechnology attractive for biotechnological and biomedical applications.

In this work, we investigated the ability of phage–AuNR bioconjugates (phage–AuNRs; Fig. 1A) to specifically attach to and then kill targeted bacterial cells via the photothermal effect. In this scheme, the phage confers specific targeting while the AuNRs

achieve the desired effect. Using chimeric phages we previously engineered (31) to target several bacterial pathogens (two strains of *Escherichia coli*, *Pseudomonas aeruginosa*, *Vibrio cholerae*, and two strains of the plant pathogen *Xanthomonas campestris*), we first show that the phage–AuNRs can be used to detect specific bacteria through phage-mediated aggregation of AuNRs on the bacterial surface, which causes a red shift of the longitudinal LSPR peak. Next, we use NIR irradiation to induce death of the targeted bacteria via photothermal heating, both in solution and in a *P. aeruginosa* biofilm grown on a substrate of mammalian epithelial cells. Photothermal lysis was highly selective and resulted in extensive killing of targeted bacteria within minutes, with low rates of damage to nontarget bacteria and mammalian cells (Fig. 1B). After photothermal lysis, the phages are no longer capable of replication, allowing control over dosage in principle. The potential of phage–AuNRs for treatment and diagnosis of antibiotic-resistant bacterial infections is discussed.

Results

Construction of Phage–AuNR Bioconjugates. The AuNRs were synthesized following a typical seed-mediated protocol (34), resulting in uniform particles with an average aspect ratio of 3.8 (average length, 53.2 nm; average width, 13.7 nm; *SI Appendix, Fig. S1A*). The UV-vis spectrum of the AuNRs demonstrated transverse and longitudinal absorption peaks at 526 and 800 nm (35), respectively (*SI Appendix, Fig. S1B*). The capsid of M13KE phage was modified with SATP to introduce thiol groups to primary amines. Thiolation resulted in new signals by Fourier-transform infrared (FTIR) spectroscopy (*SI Appendix, Fig. S2A*), indicating successful modification of the virions, designated M13KE-SH. The overall morphology of the phage, assessed by transmission electron microscopy (TEM), was not affected by thiolation (*SI Appendix, Fig. S2 B and C*).

Surface modification of gold nanostructures under aqueous conditions has been widely reported (36–38). M13KE-SH was conjugated to AuNRs by formation of gold–sulfur bonds at room temperature in Tris buffer (pH 3.0) (39). Interaction between

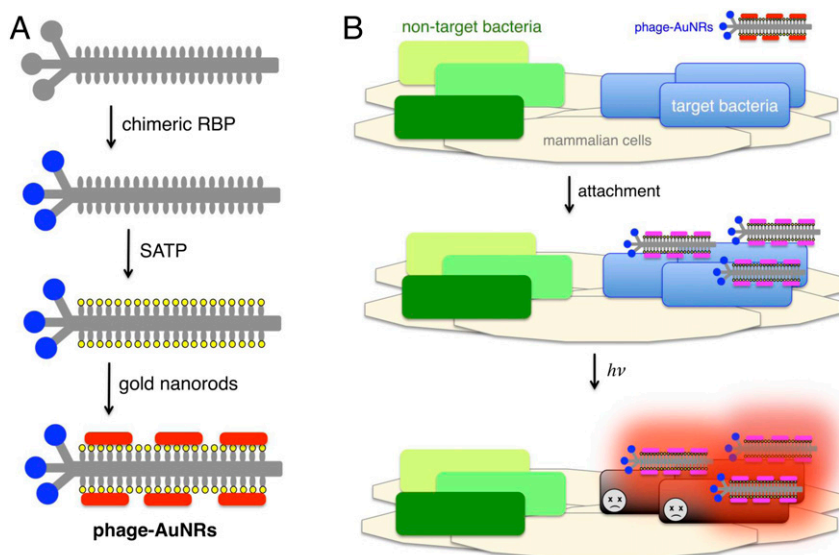


Fig. 1. Schematic of phage–AuNR bioconjugates for bacterial detection and cell killing. (A) Filamentous phage M13 (gray) was engineered to express the receptor-binding protein from a foreign phage (blue) fused to wild-type g3p to obtain retargeted chimeric phage. Chemical modification by *N*-succinimidyl-*S*-acetylthiopropionate (SATP) introduced thiol groups (yellow) along the phage coat, and gold nanorods (AuNRs) were conjugated to the phage via thiol–gold bonds. (B) Phage–AuNR bioconjugates recognize specific bacteria (blue) in the context of mammalian cells and other nontarget bacteria (green). Attachment of phage triggers AuNR aggregation on the cell surface, resulting in a red-shifted LSPR spectrum (indicated as magenta nanorods) for bacterial detection. Exposure to NIR light induces photothermal heating of AuNRs, leading to highly elevated temperatures localized by the phage, resulting in death of the targeted bacteria.

AuNRs and phages during bioconjugation was promoted by the positive charge from trace CTAB on the AuNRs ($\zeta = 21.9$ mV) and the negatively charged capsid protein of phage particles ($\zeta = -44.3$ mV). The formation of Au–S bonds in the bioconjugates was confirmed by X-ray photoelectron spectroscopy (XPS) (*SI Appendix, Fig. S1 C and D*). Trace CTAB was then replaced by ligand exchange with carboxylated PEG (HS-PEG-COOH) after bioconjugation. Formation of bioconjugates was also confirmed by TEM (Fig. 2A), which indicated ~ 10 AuNRs per phage. Another approach to estimate the ratio of AuNRs to phage particles is inductively coupled plasma mass spectrometry (ICP-MS) to measure the amount of AuNRs and qPCR to measure the amount of phage in a sample; this approach indicated ~ 20 AuNRs per phage. Thus, an estimate of the number of AuNRs conjugated per phage particle is roughly 15.

The UV-vis spectrum of the bioconjugates indicates a red shift of ~ 10 nm compared to AuNRs alone (*SI Appendix, Fig. S1B*). The negatively charged surface of HS-PEG-COOH-modified M13KE–AuNR ($\zeta = -28.8$ mV) should reduce nonspecific binding to bacteria considering the negatively charged cell surface ($\zeta = -8.88$ mV). TEM demonstrated that while HS-PEG-COOH-modified AuNRs do not attach to *E. coli* cells in the presence of nonconjugated M13KE (Fig. 2B), phage–AuNRs attach to *E. coli* cells (Fig. 2C), as expected. To further confirm that the M13KE–AuNR bioconjugates retain the ability to interact with *E. coli*, M13KE–AuNRs were labeled with a fluorescent dye using fluorescein-5-maleimide (FITC) through thiol-maleimide click chemistry, as M13KE–AuNRs contained free thiols according to the XPS spectrum (*SI Appendix, Fig. S1D*). The FITC-labeled M13KE–AuNRs were incubated with *E. coli* expressing a cyan fluorescent protein (12) and visualized by confocal microscopy, which verified close proximity of FITC and cyan fluorescence (*SI Appendix, Fig. S3*).

Having verified the method with M13KE, AuNR bioconjugates were also prepared with chimeric phages M13-g3p(If1), M13-g3p(Pf1), M13-g3p(ϕ Lf), M13-g3p(ϕ Xv), and M13-g3p(CTX ϕ), targeting *E. coli* (I^+), *P. aeruginosa*, *X. campestris* pv. *campestris*, *X. campestris* pv. *vesicatoria*, and *V. cholerae*, respectively (31) (Table 1).

Detection of Specific Bacterial Species by Phage–AuNRs. We previously reported a detection method for specific bacterial species using thiolated phages to target aggregation of gold nanoparticles (AuNPs), which causes a red shift of LSPR peaks in the UV-vis spectrum (31). In this prior work, abundant thiol groups were incorporated on carboxylates of the phage capsid (with three or more solvent-accessible residues on each g8p protein) to induce aggregation of gold nanoparticles, and removal of free thiolated phage was required to remove background signal. In the present

work, we reduced the level of thiolation of the phage surface by using amines for bioconjugation, of which there is only one solvent-accessible residue (at the N terminus) of each g8p (28). The phage–AuNRs synthesized here did not aggregate detectably in the absence of cells, but aggregation and the associated broadening and red shift of the absorbance spectrum were observed upon attachment to the target cells (Figs. 2C and 3A and *SI Appendix, Figs. S1B and S4 and Text S1*), simplifying the detection protocol to single-step addition of the bioconjugates to the cell sample in appropriate solution. *E. coli* ER2738 was suspended at varying concentrations in MilliQ water and incubated with M13KE–AuNRs for 30 min. Consistent with prior results using AuNPs, a red shift and broadening of LSPR peaks of the AuNRs were observed in the presence of $\geq 10^2$ bacterial cells (*SI Appendix, Fig. S1B*), demonstrating the sensitivity of bacterial detection using phage–AuNRs.

Five chimeric phages recognizing other Gram-negative bacterial strains (I^+ *E. coli*, *P. aeruginosa*, *V. cholerae*, and two strains of *X. campestris*) were propagated in *E. coli* cells, as previously described (31), and functionalized with AuNRs, as described above. As seen with M13KE–AuNRs targeting *E. coli* (*SI Appendix, Fig. S1B*), the sensitivity of detection for these other strains was $\sim 10^2$ CFU using the respective chimeric phage–AuNRs (Fig. 3A and *SI Appendix, Fig. S4*).

To verify the specificity of each of the six phage–AuNRs for its respective host, we incubated each phage–AuNR with the other bacterial strains. For each phage–AuNR, no shift or broadening of the LSPR peaks appeared when nonhost strains were added (Fig. 3B and *SI Appendix, Fig. S5*), indicating little cross-reactivity among the tested group of Gram-negative organisms. The detection assay was also performed in a mixture of the host strains, and no change of the LSPR peaks was observed unless the heterogeneous mixture contained the targeted host cells (Fig. 3C and *SI Appendix, Fig. S6*). These results confirm the ability of the chimeric phages to target the AuNRs to their particular bacterial host.

Photothermal Ablation of Bacterial Cells in Suspension. The plasmonic resonance of AuNRs converts light into heat, which can be used to damage and kill cells within a submicrometer to micrometer radius (40). Samples containing AuNRs or phage–AuNRs or neither were irradiated by a NIR laser (peak at 808 nm) for 10 min, and the bulk temperature of the solution was measured by a thermocouple (*SI Appendix, Fig. S7A*). In a control sample of water without AuNRs or phage–AuNRs, some heating (from 24 to 37 °C) occurred from the laser alone. However, all solutions containing AuNRs [AuNRs (equivalent to 3.3 nM AuNRs), M13KE–AuNRs (equivalent to 3.3 nM AuNRs and 10^{11} phages per mL), or M13KE–AuNRs mixed with *E. coli*

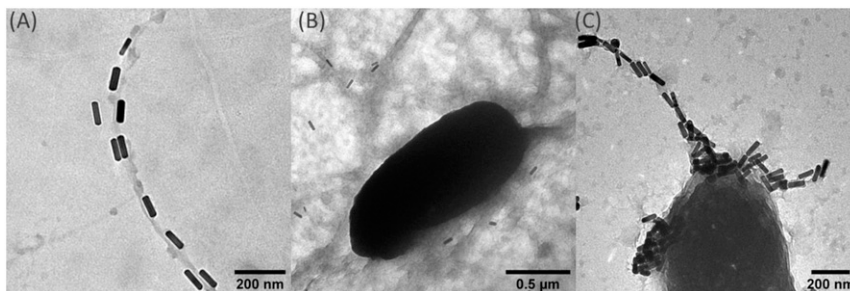


Fig. 2. Interaction between M13KE, AuNR, and *E. coli* cells. TEM image of M13KE–AuNR (A) illustrates conjugation of filamentous phage and AuNRs. When *E. coli* cells were mixed with M13KE and HOOC-PEG–AuNR (nonconjugated), no aggregation or localization of AuNRs to the cells was seen (B), but HS-PEG-COOH-modified M13KE–AuNR bioconjugates attached to *E. coli* cells did result in visible aggregation of AuNRs on the cell surface (C). Aggregation at one end of the bacterium (in C) presumably occurs near the position of the F pilus; stimulation of retraction by phage attachment may cause accumulation at the root of the pilus (57, 58).

Table 1. Chimeric phage bioconjugates and targeted bacterial species

Bacterial target strain	Source of RBP	Designation of bioconjugates
<i>E. coli</i> (F ⁺), ER2738	Wild-type M13	M13KE–AuNR
<i>V. cholerae</i> 0395	CTXφ	M13-g3p(CTXφ)–AuNR
<i>E. coli</i> (I ⁺), (Migula) Castellani and Chalmers	If1	M13-g3p(If1)–AuNR
<i>X. campestris</i> (pv. <i>campestris</i>)	φLf	M13-g3p(φLf)–AuNR
<i>X. campestris</i> (pv. <i>vesicatoria</i>)	φXv	M13-g3p(φXv)–AuNR
<i>P. aeruginosa</i> (Schroeter) Migula	Pf1	M13-g3p(Pf1)–AuNR

See ref. 31 for additional details.

ER2738 (10⁶ cells per mL)] reached bulk temperatures of 77 to 81 °C. A sample containing M13KE–AuNRs alone reached 81 °C, while a sample containing M13KE–AuNR mixed with *E. coli* reached a lower temperature (77 °C). This slight reduction is expected due to the aggregation of M13KE–AuNRs on the cells (see preceding section). That is, since aggregation leads to a broadened and red-shifted LSPR peak, absorption at the laser wavelength (808 nm) is reduced (SI Appendix, Fig. S7B) and leads to slightly less efficient heating when phage–AuNRs are aggregated on the target cells. Plating of samples containing M13KE–AuNRs mixed with *E. coli* ER2738 and irradiated demonstrated that roughly 50% of bacteria were killed by 3 min, ~80% of bacteria were killed by 6 min, and no viable bacteria remained after 10 min (Fig. 4 A and C). Similar results were observed using all six phage–AuNR bioconjugates to kill their respective host bacterial cells (Fig. 4 B and C and SI Appendix, Fig. S8). TEM imaging of M13KE–AuNRs mixed with *E. coli* ER2738 cells and irradiated demonstrated grossly altered cell morphology (SI Appendix, Fig. S9A). A live/dead cell-staining assay further verified >99% bacterial cell death after 10 min of irradiation by microscopy (SI Appendix, Fig. S10).

In principle, cell death should occur primarily for the targeted host organism bound by the phage–AuNRs. However, nontargeted cells may also die as the temperature of the bulk solution increases or if they are bound nonspecifically by phage–AuNRs. As expected, irradiation of bacteria with nonconjugated AuNRs resulted in gradual cell death (SI Appendix, Fig. S11), presumably from bulk heating of the solution by irradiated AuNRs, and this rate of cell death was substantially slower than the rate of death using targeted phage–AuNRs (Fig. 4C). Irradiated bacteria (without AuNRs) showed no significant cell death compared to nonirradiated bacteria, indicating that irradiation alone is not toxic (SI Appendix, Fig.

S12). To test the efficiency and specificity of bacterial cell death in the context of a bacterial mixture, F⁺ *E. coli* cells (ER2738; host for M13KE) that express cyan fluorescent protein (10⁶ cells per mL) were mixed with F[−] *E. coli* cells (BL21; lacks receptor for M13KE) that express citrine fluorescent protein (10⁶ cells per mL), incubated with M13KE–AuNRs (10¹¹ phages per mL), and irradiated to induce photothermal lysis (12). Samples were plated and viable colonies were counted. The concentration of F⁺ *E. coli* (targeted strain) decreased sharply, with no colony-forming units at 10 min (Fig. 4D and SI Appendix, Fig. S13). In contrast, the concentration of F[−] *E. coli* (nontarget strain) changed only slightly compared to control (Fig. 4D and SI Appendix, Fig. S13). This confirms that the phage–AuNRs distinguished bacterial strains as expected and selectively killed the targeted cells.

While the bulk temperature increases upon irradiation, binding of phage–AuNRs to bacterial cells should induce localized heating of the cell. To estimate the temperature of the bacteria, *E. coli* ER2738 were stained with the temperature- and pH-sensitive dye BCECF, whose fluorescence intensity decreases linearly with temperature (SI Appendix, Fig. S9 B and C). The steady-state fluorescence intensity of BCECF was recorded during irradiation of *E. coli* ER2738 with M13KE–AuNRs. The apparent cell temperature reached a plateau of ~83 °C after 3 min and rose more quickly than the bulk temperature, being higher than the bulk temperature at all observed time points. The temperature gap between cell temperature and bulk temperature (measured by thermocouple) was observed to be ~13 °C at 3 min (SI Appendix, Fig. S9D). It should be noted that bulk heating observed depends on the concentration of AuNRs as well as heat dissipation properties of the medium and cuvette. The BCECF measurement is also likely to underestimate the true bacterial cell temperature since some dye is also dissolved in the bulk; thus, it should be

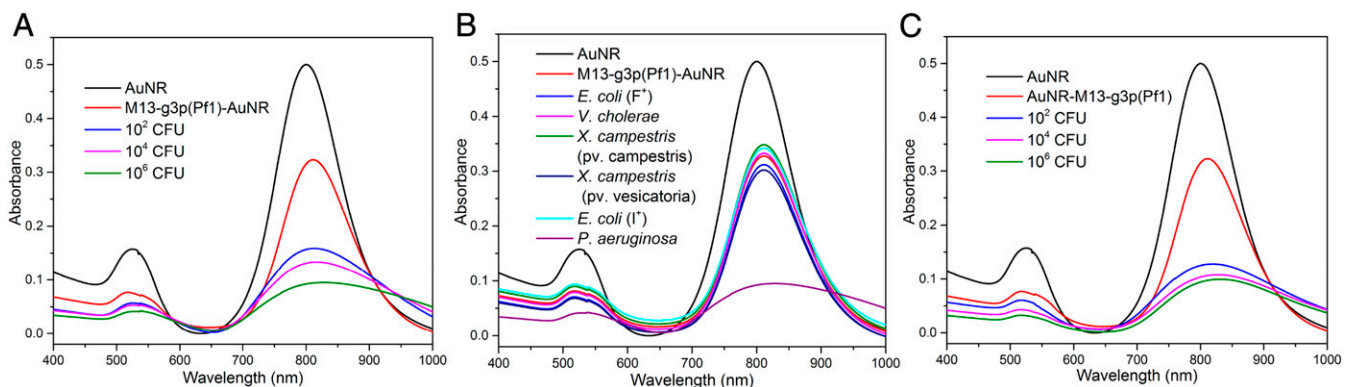


Fig. 3. Detection of *P. aeruginosa*. (A) UV-vis spectra of AuNR (black), phage–AuNR (red), and phage–AuNR with *P. aeruginosa* at 10², 10⁴, and 10⁶ CFU (blue, magenta, and green lines, respectively) are shown; (B) Specificity of *P. aeruginosa* detection when incubated with different bacterial species (10⁶ CFU). Bacterial species shown are *E. coli* (F⁺) (blue), *V. cholerae* (magenta), *X. campestris* (pv. *campestris*) (green), *X. campestris* (pv. *vesicatoria*) (navy), *E. coli* (I⁺) (cyan), and *P. aeruginosa* (purple). (C) Sensitivity of *P. aeruginosa* detection in the context of a mixture of bacteria [*E. coli* (F⁺), *V. cholerae*, *X. campestris* (pv. *vesicatoria*), *X. campestris* (pv. *campestris*), and *E. coli* (I⁺)]. The target cells *P. aeruginosa* were present in the amount indicated in the legend [10² (blue), 10⁴ (magenta), 10⁶ (green) CFU]; the other bacterial species were present at 10⁶ CFU each. The spectra of AuNRs (black) and M13-g3p(Pf1)–AuNR bioconjugates (red) are also shown.

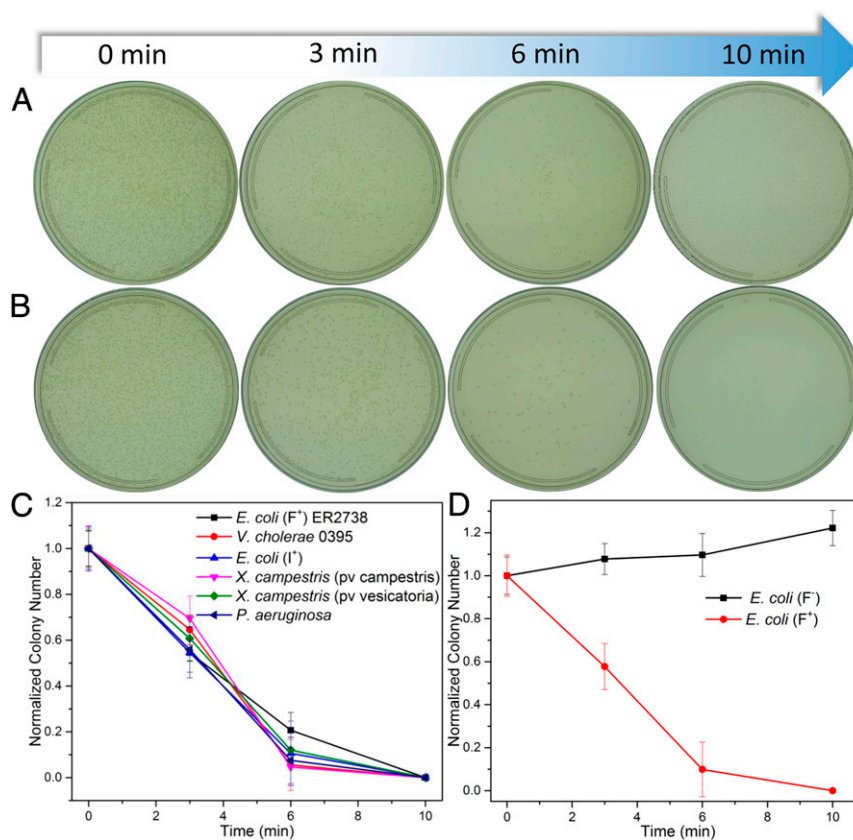


Fig. 4. Photographs of (A) *E. coli* (F⁺) ER2738 and (B) *P. aeruginosa* plated on LB plates after different NIR irradiation times; C and D show loss of colony-forming units at different irradiation time points (normalized to a control with bacteria mixed with nonconjugated AuNRs and irradiated for the same time; *SI Appendix, Fig. S11*). Error bars show 1 SD calculated from three or more replicates. Absence of visible error bars indicates no deviation among sample measurements (0 colonies).

regarded as a lower bound for bacterial cell temperature. In addition, pH is assumed to be constant during irradiation, such that the fluorescence change is attributed to temperature changes. Nevertheless, this measurement validates the qualitative expectation that the targeted cells are heated beyond the level of the bulk solution.

Photothermal Ablation of *P. aeruginosa* in Biofilms. Biofilms present an important obstacle to antibiotics and other therapeutic strategies due to the dense macromolecular network and altered physiological state of the biofilm cells. To determine whether photothermal ablation could be effective against bacterial biofilms, we grew *P. aeruginosa* in a standard biofilm format on glass-bottom plates (41), incubated the biofilm with M13-g3p(Pf1)-AuNRs (10^{13} phages per mL), removed excess liquid by pipetting, and irradiated as described above for 10 min. Live/dead staining of the biofilm showed widespread bacterial cell death (Fig. 5A and B). The green dye SYTO 9 enters both live and dead cells, while the red dye propidium iodide (PI) only enters compromised cell membranes (dead cells). Object-based colocalization analysis was used to determine the fraction of cells (green) that also stained red; this analysis confirmed extensive cell death (Fig. 5A and B and *SI Appendix, Fig. S14*). In addition, no colonies were obtained after resuspension and plating of the irradiated biofilm (*SI Appendix, Fig. S15*), indicating that no viable cells remained. The extent of cell death during irradiation was also quantified by the PrestoBlue cell viability assay, which confirmed that viable cells were undetectable after 10 min of irradiation (Fig. 5C).

To assess the effectiveness of phage-AuNRs against more mature biofilms, we grew *P. aeruginosa* biofilms for longer times (24 and 48 h), resulting in increased extracellular polymeric substance (EPS) formation verified by crystal violet staining (*SI Appendix, Fig. S16*). Cell killing was slightly slower for more mature biofilms, but still there was no detectable viability after 10 min of irradiation (Fig. 5C).

To gain a rough estimate of the temperature of the biofilm after NIR irradiation, the biofilms were stained with BCECF. To create a calibration curve, a series of fluorescent images was recorded at different temperatures using a confocal microscope (*SI Appendix, Fig. S17A*), and the pixel intensity (measured by ImageJ) was plotted as a function of temperature (*SI Appendix, Fig. S17B*). The average bacterial cell temperature captured a few seconds after 10 min of NIR irradiation was estimated to be 84 °C using this calibration curve (*SI Appendix, Fig. S17C*), indicating similarly efficient heat transfer from the AuNRs to bacterial cells in the biofilm compared to solution.

Photothermal Ablation of *P. aeruginosa* Biofilm Grown on Mammalian Epithelial Cells. While phage-AuNR-mediated heating was effective for killing bacterial cells, it is possible that heat transfer to surrounding mammalian cells could be deleterious. We grew a *P. aeruginosa* biofilm directly on top of a monolayer of Madin-Darby Canine Kidney II (MDCKII) mammalian epithelial cells (42) and determined the survival of both the bacterial cells and the MDCKII cells after application of M13-g3p(Pf1)-AuNRs with irradiation performed as described above. Microscopy with live/dead staining demonstrated that bacterial cells in the biofilm were killed while MDCKII cells survived, with extensive (~98%)

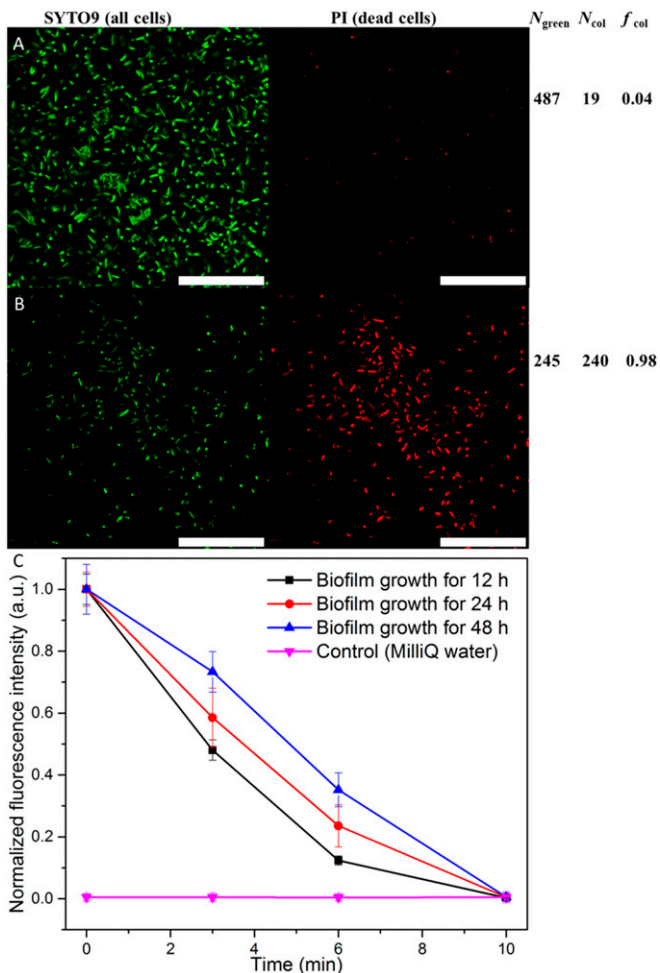


Fig. 5. Treatment of *P. aeruginosa* biofilm by M13-g3p(Pf1)-AuNRs and NIR irradiation. Live/dead cell staining assay of *P. aeruginosa* biofilm (A) before and (B) after 10-min irradiation. From Left to Right are green field (SYTO 9: all cells) and red field (PI: dead cells). f_{col} is the fraction of cells identified as dead, $= N_{col}/N_{green}$, where N_{green} is the number of green objects counted and N_{col} is the number of green objects whose centers colocalize with the center of a red object (JACoP, version 2.0/ImageJ). Also see *SI Appendix, Fig. S14*. (Scale bar: 30 μm .) (C) PrestoBlue cell viability results for biofilms grown for 12 to 48 h (fluorescence indicates reducing potential and thus quantity of living cells). Fluorescence was normalized by the average initial fluorescence of the samples before irradiation; the control is MilliQ water.

bacterial cell death by 10 min (Fig. 6 and *SI Appendix, Figs. S18 and S19*). This result was verified by a PrestoBlue cell viability assay (Fig. 7A), which indicated that nearly all bacterial cells were killed by incubation with M13-g3p(Pf1)-AuNRs and 10 min of irradiation at the laser power used (3.0 W/cm²). The viability of MDCKII cells without biofilm was reduced to ~71% by application of M13-g3p(Pf1)-AuNRs and irradiation for 10 min, compared to MDCKII cells before exposure to M13-g3p(Pf1)-AuNRs or irradiation (Fig. 7A, blue line). Interestingly, when the MDCKII cells were covered by a *P. aeruginosa* biofilm, a greater proportion of the MDCKII cells appeared to survive application of M13-g3p(Pf1)-AuNRs and irradiation for 10 min (~84% viability; Fig. 7A, red line), as determined by PrestoBlue assay. The fluorescence of the MDCKII cells covered by biofilm, treated, and irradiated for 10 min, could be attributed to the MDCKII cells because negligible fluorescence intensity was observed for an identically treated and irradiated bacterial biofilm without MDCKII cells (Fig. 7A, black line). This protective effect could be due to the biofilm adsorbing the M13-g3p(Pf1)-AuNRs, leading to less

nonspecific binding of the bioconjugates to MDCKII cells and/or to a reduction of laser fluence reaching the MDCKII cells due to absorption by the greater number of bioconjugates in the biofilm. Regardless, these results demonstrated survival of the majority of mammalian cells while few (if any) bacterial cells survived; optimization of the irradiation protocol may enhance this difference. Furthermore, the phages and bioconjugates themselves (without irradiation) were nontoxic to MDCKII cells in a broad concentration range, as demonstrated by the PrestoBlue cell viability assay (Fig. 7B).

To further probe the effect of phage-AuNRs on the bacteria and MDCKII cells, we characterized the viscosity of cell membranes using a molecular rotor, a dye whose fluorescence lifetime provides a measurement of local microviscosity. The viscosity of the cell membrane is expected to decrease upon intense heating, leading to destruction of membrane order. We stained the MDCKII/*P. aeruginosa* biofilm with the molecular rotor BODIPY C10 and used fluorescence lifetime imaging (FLIM) (43) to assess membrane viscosities after photothermal treatment (Fig. 8 and *SI Appendix, Fig. S20*). While the MDCKII cells did not exhibit substantial change in fluorescence lifetime after irradiation (2.31 ± 0.17 ns before irradiation; 2.23 ± 0.21 ns after irradiation), the fluorescence lifetime of the dye on *P. aeruginosa* cells decreased from an average of 2.36 ± 0.12 to 0.92 ± 0.09 ns, corresponding to a dramatic drop in viscosity from 296 to 38 cP (see Eq. 1). This finding is consistent with the idea that the phage-AuNRs directly target the bacterial host cells with relatively little damage to other cells.

To verify whether NIR irradiation destroyed the infectious potential of the phages, M13KE-AuNRs were irradiated for 10 min and then used to infect *E. coli* for phage propagation. Putative viral DNA was extracted and assayed by qPCR (31). No DNA was detected from propagation of the treated sample (*SI Appendix, Fig. S21*), confirming that the phages were inactivated during the treatment.

Comparison to AuNRs Conjugated to Anti-LPS Antibodies. The optical and cell-killing properties of M13KE-AuNRs were compared to those of AuNRs conjugated to a commercially available monoclonal antibody against the lipopolysaccharide (LPS) of *E. coli* ($\alpha\text{LPS-AuNRs}$; *SI Appendix, Methods*). In these experiments, the concentration of AuNRs was kept constant between samples with M13KE-AuNRs and samples with $\alpha\text{LPS-AuNRs}$. Attachment of $\alpha\text{LPS-AuNRs}$ to *E. coli* was verified by TEM (*SI Appendix, Fig. S22 A and B*). During photothermal ablation in solution, $\alpha\text{LPS-AuNRs}$ killed cells significantly more slowly than M13KE-AuNRs (50% of cells killed after ~6 min of irradiation for $\alpha\text{LPS-AuNRs}$ compared to <3 min for M13KE-AuNRs) (*SI Appendix, Fig. S23A*). The cell-killing activity of the conjugates against target cells in the context of a large excess of nontarget cells was also compared for M13KE-AuNRs vs. $\alpha\text{LPS-AuNRs}$. We mixed F⁺ *E. coli* (target) with F⁻ *E. coli* (nontarget) in a frequency of 10^{-6} . In the mixture, irradiation with M13KE-AuNRs eradicated the F⁺ cells (no detected colonies) while leaving most F⁻ cells alive, as expected. However, $\alpha\text{LPS-AuNRs}$, which are not expected to discriminate between F⁺ and F⁻ cells, indeed killed both types of cells to the same degree. Moreover, $\alpha\text{LPS-AuNRs}$ were not able to eradicate either cell type, with ~30% of cells surviving (*SI Appendix, Fig. S23B*).

The LSPR spectral shift was also compared for $\alpha\text{LPS-AuNRs}$ vs. M13KE-AuNRs. $\alpha\text{LPS-AuNRs}$ show a spectral shift with a similar limit of detection (LOD ~ 10^2 CFU) as M13KE-AuNRs at neutral pH (*SI Appendix, Fig. S22*). However, M13KE-AuNRs tolerated both acidic and alkaline conditions (pH 3 and pH 10), but the LOD of $\alpha\text{LPS-AuNRs}$ increased by 4 orders of magnitude under these conditions. In addition, M13KE-AuNRs tolerated heat treatment (60 °C for 15 min) while $\alpha\text{LPS-AuNRs}$ did

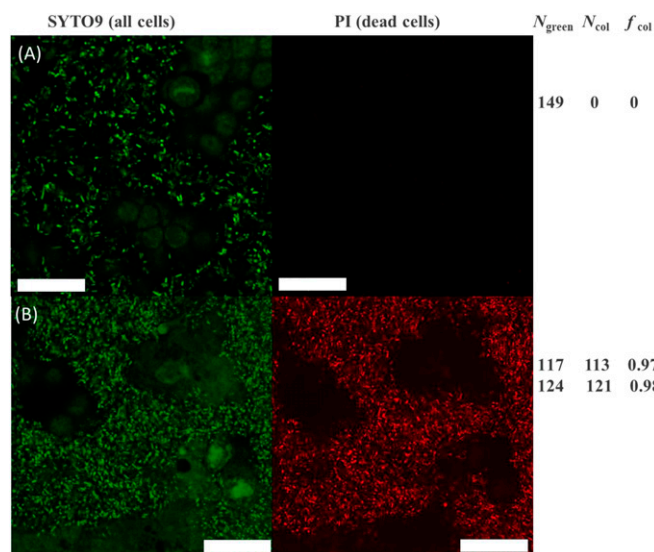


Fig. 6. Live/dead cell staining assay of *P. aeruginosa* biofilm grown on MDCKII cells, treated with M13-g3p(Pf1)-AuNRs, before (row A) and after (row B) 10 min of NIR irradiation. From Left to Right are green field (SYTO 9: all cells) and red field (PI: dead cells). See Fig. 5 for explanation of N_{green} , N_{col} , and f_{col} . In B, because stained MDCKII nuclei interfered with object detection, two regions were chosen from the larger image, which avoided overlap with MDCKII nuclei. Counts are given for both regions. Also see *SI Appendix*, Fig. S18. (Scale bar: 30 μm .)

not (LOD increased by 2 orders of magnitude). In acidic and alkaline (pH 3 and pH 10) conditions, cell killing by M13KE-AuNRs was maintained at high efficiency while αLPS -AuNRs lost activity (*SI Appendix*, Fig. S23A). These observations are consistent with the fact that many factors (e.g., temperature, pH, ionic strength, growth media) can disrupt the antigen-antibody interaction (44–46), while phage-host interactions appear to be more robust to environmental factors.

Discussion

We present an antibacterial strategy using phages conjugated to AuNRs (phage-AuNRs, referred to in the following discussion as “phanorods,” a portmanteau of “phage” and “nanorods”). The phages attach to targeted bacteria, and irradiation of the nanorods by NIR light causes LSPR excitation. This energy is released as heat, destroying the phage as well as bacteria bound to the phage. The phanorod strategy has important advantages over traditional approaches to phage therapy. First, phage therapy suffers from the major difficulty of managing a replicating and evolvable entity. While the evolutionary capacity of phages is advantageous for overcoming bacterial resistance against a phage, evolutionary potential is an important biocontainment concern in practice. Second, nonlinear replication dynamics mean that dosages cannot be easily controlled, which may be problematic if cell lysis releases endotoxins triggering deleterious host responses (e.g., septic shock). Phanorods are destroyed during irradiation, preventing replication and evolution during treatment and enabling control over dosage. Irradiation could also be used to inactivate excess phanorods after use, avoiding negative impacts, such as evolution of resistant organisms, currently associated with antibiotics in the waste stream. Third, evolution of resistance is an important challenge for any antibacterial strategy, including phanorods. However, because the phage is used only for attachment to cells and downstream events (e.g., replication) are not relevant, bacterial mechanisms for resistance should be limited to alterations of the receptor, presenting a smaller mutational target for evolution of resistance. Fourth, phanorods serve simultaneously as diagnosis and cytotoxic reagents, as the change in the LSPR spectrum can be used to recognize bacterial species. Therefore, although there may be situations in which therapy with phages per se is desired (e.g., if exponential replication dynamics are needed), phanorod pharmacokinetics and pharmacodynamics may more closely resemble those of a typical drug rather than a living organism, which would be advantageous for most therapeutic situations.

Conversely, one may consider how phanorods compare to antibody-conjugated nanorods. In addition to unique search mechanisms (see Introduction), phages can possess very high affinities

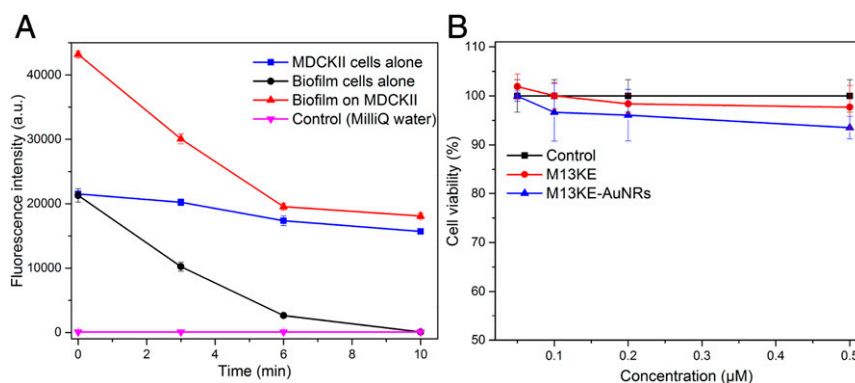


Fig. 7. Treatment of *P. aeruginosa* biofilm grown on MDCKII cells using M13-g3p(Pf1)-AuNRs and biocompatibility of phage-AuNRs with MDCKII cells. (A) PrestoBlue cell viability assay results for M13-g3p(Pf1)-AuNR treatment and irradiation of MDCKII cells grown alone (blue), M13-g3p(Pf1)-AuNR treatment and irradiation of *P. aeruginosa* biofilm grown on MDCKII cells (red), and M13-g3p(Pf1)-AuNR treatment and irradiation of *P. aeruginosa* biofilm alone (grown without MDCKII cells; black), over time during irradiation. The control (magenta) is MilliQ water alone. In this assay, the PrestoBlue reagent is modified by the reducing environment of live cells and becomes fluorescent; both MDCKII and *P. aeruginosa* cells contribute to PrestoBlue fluorescence. MDCKII cells (blue) are largely viable upon M13-g3p(Pf1)-AuNR treatment and irradiation, while *P. aeruginosa* cells (black) are killed by M13-g3p(Pf1)-AuNR treatment and irradiation over the time course shown. As expected, the PrestoBlue fluorescence of the biofilm grown on MDCKII cells during M13-g3p(Pf1)-AuNR treatment and irradiation (red) is roughly equal to the sum of the fluorescence of MDCKII cells treated and irradiated alone (blue) plus the fluorescence of biofilm cells treated and irradiated alone (black). After 6 min of treatment and irradiation, the fluorescence of the biofilm grown on MDCKII cells (red) appears to be similar to that of MDCKII cells alone (treated and irradiated; blue), consistent with selective killing of *P. aeruginosa*. (B) Biocompatibility of phage-AuNRs was measured by PrestoBlue cell viability assay. M13KE-AuNRs or M13KE phages at different concentrations were incubated with MDCKII cells for 48 h without irradiation. The control is MDCKII cells alone (without M13KE-AuNRs or M13KE). Cell viability percentages were calculated by normalizing fluorescence intensity by the control fluorescence. The concentration of the bioconjugates and phages are given in units of micromolar concentration (1 $\mu\text{M} \sim 6 \times 10^{14}$ phage particles per mL). Error bars represent 1 SD calculated from triplicates.

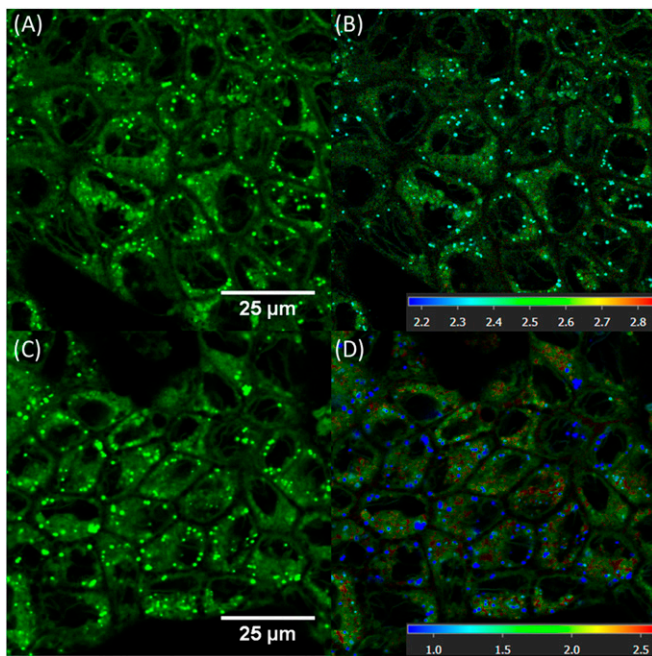


Fig. 8. Confocal microscopy (single representative section; *Left*) and FLIM (*Right*) images of *P. aeruginosa* biofilm on MDCKII cells, stained with the fluorescent molecular rotor BODIPY C10, before (*A* and *B*) and after (*C* and *D*) treatment with M13-g3p(Pf1)-AuNRs and 10 min of NIR irradiation. Bacterial cells appear as bright green (*A* and *C*) or cyan/blue (*B* and *D*) spots. False color scale (*B* and *D*) represents fluorescence lifetime in nanoseconds.

to their targets. For example, the affinity of M13KE for F⁺ *E. coli* is 2 pM (12), which is several orders of magnitude greater than the affinities of antibodies reported against F pilin (47) and also higher than affinities of most antibodies isolated from mice (30 to 500 pM, with those at low picomolar affinity being quite rare) (48, 49). In the experimental comparison done here between M13KE-AuNRs and α LPS-AuNRs, we found that M13KE-AuNRs indeed outperformed α LPS-AuNRs in photothermal ablation experiments, despite the greater amount of LPS present on the cell surface compared to the F pilus. It may be of particular interest to eradicate targeted bacteria in small numbers, such as “persister” cell populations that escape other treatment modalities (50). In such applications, the very high affinities and often high specificities of phages would avoid competition for binding by nontarget cells and thus prevent loss of phanorod activity compared to α LPS-AuNRs, as demonstrated here in a mixed bacterial population. The experiments also confirmed the environmental hardiness of the phanorods, which, unlike the α LPS-AuNRs, tolerated the range of pH tested (pH 3 to 10) as well as heat treatment. We speculate that very high affinities and “hunting” strategies for bacteria, environmental hardiness, and tolerance to mutations and thus chemical modification, which characterize phages, are traits under selection by the ongoing evolutionary “arms race” between bacteria and phages (51). This constellation of traits is advantageous for therapeutic nanomaterials and may be unique to phages.

The phanorod strategy presented here is best suited for treatment of directly accessible tissues or surfaces. Near-term applications could be localized topical therapy, particularly for wound infections or colonization of medical devices, in which the phage-nanorods can be directly applied to the biofilm. For example, while *P. aeruginosa* is well known as a pulmonary pathogen, drug-resistant *P. aeruginosa* is also a major pathogen in chronic wounds (52), surgical site infections, and burns (53). Such wounds would be directly accessible for application of therapeutic nanomaterials and NIR irradiation.

Bacterial biofilms represent a difficult challenge (54) for treatment, as the protective extracellular matrix often inhibits access by antibiotics. However, heat can be transferred without molecular penetration into the biofilm. While the phanorod strategy should be generalizable to different bacterial strains depending on the creation of chimeric phages, we focused on *P. aeruginosa* as one of three “critical priority” bacterial pathogens identified by the World Health Organization (55). In this work, we demonstrated that phanorods were effective in killing a *P. aeruginosa* biofilm grown on epithelial cell culture (see *SI Appendix, Text S2* for further discussion). Some photothermal damage was incurred by epithelial cells, although the viability measured here is likely a lower bound since the biofilm was in direct contact with the monolayer; underlying cellular layers in a physiological context would likely sustain less damage. The phanorods used here absorb in the relatively biologically transparent window of NIR light. In principle, irradiation could be directed only toward areas where activation of the phanorods is desired, reducing potential side effects. Whether iterative phanorod application could be effective in treating thicker and deeper biofilms (e.g., abscesses) without substantial harm to surrounding tissue is an important practical issue. In addition, while excess phanorods could be removed by washing for certain wounds, a consideration for other applications is the *in vivo* biodistribution of phanorods in the absence of target bacteria. Nevertheless, phanorods and other alternative strategies merit consideration given the current need to develop new antibiotic agents.

Methods

Materials. Reagents were obtained from the following sources: gold(III) chloride trihydrate (HAuCl₃•3H₂O) (99.9%; Sigma), sodium borohydride (NaBH₄) (98%; Fisher Scientific), trisodium citrate dihydrate (99.9%; Sigma), *Escherichia coli* (Migula) Castellani and Chalmers (ATCC27065, ATCC), *E. coli* ER2738 (NEB), *Xanthomonas campestris* pv. *campestris* (ATCC33913), *Xanthomonas campestris* pv. *vesicatoria* (ATCC35937), *Pseudomonas aeruginosa* (Schroeter) Migula (ATCC 25102), *Vibrio cholerae* 0395 (donation from Dr. Michael J. Mahan, University of California, Santa Barbara, CA), M13KE phage (NEB), M13-NotI-Kan construct (12), sodium chloride (NaCl) (99%; Fisher BioReagents), tryptone (99%; Fisher BioReagents), yeast extract (99%; Fisher BioReagents), *E. coli* ER2738 (NEB), fluorescein-5-maleimide (97%; TCI), *N*-succinimidyl-5-acetylthiopropionate (SATP) (Thermo Fisher Scientific), hydroxylamine hydrochloride (99%; Sigma), *N*-(3-dimethylaminopropyl)-*N'*-ethylcarbodiimide hydrochloride (EDC) (99.9%; Sigma), *N*-hydroxysuccinimide (NHS) (98%; Sigma), mouse monoclonal anti-*E. coli* LPS antibody ([2D7/1] ab35654; Abcam), 2',7'-bis-(2-carboxyethyl)-5-(and-6)-carboxyfluorescein (BCECF) (Invitrogen), 5-bromosalicylic acid (5-BAA) (>98.0%; TCI), SYTO 9, PI (Thermo Fisher Scientific), BODIPY C10 (donation from Dr. M. Kuimova from Imperial College London, London, UK), poly(ethylene glycol) (PEG-8000; Sigma), dialysis kit (MWCO 3500 Da; Spectrum Labs), tetracycline (98%; Fisher Scientific), kanamycin sulfate (98%; Fisher Scientific), ampicillin (98%; Fisher Scientific), isopropyl β -D-1-thiogalactopyranoside (IPTG) (99%; Fisher Scientific), Mix & Go competent cells (Zymo Research), QIAprep Spin Miniprep Kit (Qiagen), QIAquick Gel Extraction Kit (Qiagen), KpnI-HF/NotI-HF restriction enzyme and T4 DNA ligase (NEB), and thiol-PEG-acid (HOOC-PEG-SH; PEG average M_n 5,000; Sigma).

Chimeric Phages. The construction of the chimeric phages used here [M13-g3p(CTX ϕ), M13-g3p(Pf1), M13-g3p(ϕ Lf), M13-g3p(ϕ Xv), and M13-g3p(If1)] was previously reported (31). Phages were propagated according to standard protocols. Phage concentrations were quantified by real-time PCR as previously described (31). See *SI Appendix* for more details.

Thiol Functionalization of Phages. Phages were treated with SATP for chemical modification of accessible amine groups of the capsid based on a known protocol (56). See *SI Appendix* for more details.

Synthesis of AuNRs. The AuNRs were synthesized through a modified method by Murray and coworkers (34). See *SI Appendix* for more details.

Preparation of Phage-AuNR Bioconjugates. Conjugation of thiolated phage with AuNRs was conducted based on a known bioconjugation method (39).

The AuNRs were resuspended in Tris buffer (50 mM, pH 3). Two hundred microliters of thiolated phage (1×10^{11} pfu/mL) was added dropwise to 1-mL AuNRs solution (6.8 nM). The suspension was incubated at room temperature for 2 h under moderate rotation. The phage–AuNR conjugates were purified by repeated centrifugation/resuspension cycles (8,000 rpm for 30 min, resuspension in 1 mL of water). The reaction was monitored by UV-vis spectrophotometer (Shimadzu UV-1800) and Zetasizer APS (Malvern) to follow changes of LSPR and zeta potential. The trace amount of residual CTAB was further exchanged with HOOC-PEG-SH (2.0 μ M) under the same conditions for 24 h. The phage–AuNR bioconjugates were purified by centrifugation and resuspended in 200 μ L of water.

Visualization of Binding of M13KE–AuNR to *E. coli*. 10^{11} M13KE–AuNR bioconjugates (i.e., containing 10^{11} M13KE phages) were incubated with 2 mg/mL fluorescein-5-maleimide in 1 mL of PBS buffer (pH 7.0) with gentle stirring at room temperature overnight. The free dye was removed by extensive dialysis (MWCO 3,500 Da) in 500 mL of PBS buffer (pH 7.0), and bioconjugates were concentrated by ultrafiltration to ~ 200 μ L with an Amicon Ultra-4 10000 filter. The M13KE–AuNR bioconjugates were incubated with 1 mL of Top 10F' cells expressing cyan fluorescent protein at an optical density ~ 0.6 for 30 min at room temperature (12). Free bioconjugates were removed by centrifugation at 5,000 rpm and discarding the supernatant. The pellet was washed by PBS buffer twice and resuspended in 1 mL of PBS buffer for microscopy. The fluorescence images were recorded on a Leica SP8 confocal microscope (Leica), with excitation at 405 nm.

Detection of Bacteria with Phage–AuNR. Bacterial cells (strains of *E. coli*, *V. cholerae*, *P. aeruginosa*, and *X. campestris* listed above) were grown in liquid culture and cell concentrations estimated by optical density as previously described (31) (SI Appendix, Methods). The cells were collected by centrifugation and resuspended in MilliQ water at the desired concentrations. Fifty microliters of bacterial solution was added into 100 μ L of phage–AuNR bioconjugate solution ($\sim 10^{11}$ phage particles per mL) in 1.5-mL tubes. The absorbance of the solutions was recorded by UV-vis spectroscopy (Shimadzu UV-1800) after a 30-min incubation at room temperature. The specificity of detection was tested by adding a different bacterial species or strain from the host of the phage source of the g3p-N homolog (Table 1), or by adding a mixture of host cells [*E. coli* (F⁺), *V. cholerae* 0395, *E. coli* (I⁺), *X. campestris* (pv campestris), *X. campestris* (pv vesicatoria), and *P. aeruginosa*] for the assay.

Photothermal Lysis of Bacteria with Phage–AuNRs. To test thermolysis in aqueous solution, the mixture of bacterial solution and phage–AuNRs (10^{11} phages, and 10^6 cells in 1 mL solution) was irradiated for various time periods (0 to 10 min) using an 808-nm diode laser (3.0 W/cm²; Q-BALHE Company) ~ 8 cm from the top of the solution. After irradiation, a 10- μ L aliquot of the resulting solution was diluted into PBS buffer (0.1 M, pH 7.4) to a ratio of 1:1,000 and cultured on plates for colony counting using ImageJ. *X. campestris* (pv campestris) and *X. campestris* (pv vesicatoria) were cultured on YPD agar plates with no antibiotics; the other cells were cultured on LB plates. *E. coli* ER2738 was cultured on LB plates containing 10 μ g/mL tetracycline. The *E. coli* strains expressing cyan or citrine fluorescent proteins (12) were cultured on LB plates containing 1 mM IPTG and 100 μ g/mL ampicillin.

To test thermolysis of a *P. aeruginosa* biofilm grown on solid support, the biofilm was prepared using a protocol modified from the literature (41). A single colony of *P. aeruginosa* was selected and grown in LB overnight at 37 °C in a shaker incubator. The overnight culture was diluted 100-fold into fresh medium. One hundred fifty microliters of the dilution was added to Lab-Tek plates (culture area, 0.7 cm²) and incubated overnight at 37 °C. After incubation, the liquid was removed by turning the plate over and shaking out the liquid. The remaining biofilm was washed by submerging the plate in a small tub of water and shaking out water twice. Three hundred microliters of M13-g3p(Pf1)–AuNR bioconjugates (10^{13} phages per mL) were added into the biofilm and incubated for 30 min. Unbound bioconjugates in suspension were removed by pipetting. The biofilm was irradiated with the NIR laser for 10 min as described above. Cell viability was studied by growing the resuspended bacteria on LB plates (1 μ L of cell suspension was diluted in 1 mL of PBS buffer, and 5 μ L of the dilution was plated onto LB plates) for colony counting, and by confocal microscopy with live/dead cell viability staining with SYTO9 and PI.

To test thermolysis of a *P. aeruginosa* biofilm grown on mammalian epithelial cells, wild-type MDCKII epithelial cells in suspension were seeded at 5.0×10^4 cells per well in eight-well chamber slide Lab-Tek plates and grown to confluency. Dulbecco's modified Eagle's medium (DMEM) (Thermo Fisher;

11885076) was supplemented with 10% FBS (Thermo Fisher; 10437036) and 1% penicillin–streptomycin (P/S) (Thermo Fisher; 15140122), and kept in an incubator at 37 °C with 5% CO₂. After 48 h, the culture medium was removed, and the cells were washed twice with PBS buffer to remove traces of P/S. The biofilm of *P. aeruginosa* was cultured on the top of the MDCKII epithelial cells in 15 mM Hepes buffer (pH 7 with DMEM and 10% FBS) as described above. Planktonic cells were removed from the biofilm by careful pipetting. Incubation with M13-g3p(Pf1)–AuNR (10^{13} phages per mL) and NIR irradiation of the bacterial cells was performed as described above. Cell viability of the MDCKII cells was assayed by the PrestoBlue cell viability assay, and bacterial and mammalian cells were assessed by confocal microscopy with live/dead cell viability staining with SYTO9 and PI.

Cytotoxicity of Phage and Phage–AuNR. The PrestoBlue cell viability assay was performed according to the manufacturer's protocol (Invitrogen). MDCKII epithelial cells were cultured to confluency in a 96-well microtiter plate as described above. After 24 h, the medium was replaced by 180 μ L of fresh DMEM (containing 10% FBS) with 20 μ L of samples of various concentrations of M13KE phage or phage–AuNR bioconjugates in PBS buffer. The cells were incubated for another 48 h, and the medium was replaced by 90 μ L of fresh medium, mixed with 10 μ L of PrestoBlue. The cells were incubated at 37 °C for 30 min, and fluorescence signals were measured on a TECAN infinite 200 Pro plate reader (TECAN). The excitation wavelength was 560 nm (bandwidth, 9 nm), and the emission wavelength was 600 nm (bandwidth, 20 nm). Similar results were obtained using a 1-h incubation time. The cell viability was expressed as a percentage relative to the control cells (MDCKII cells incubated with PBS buffer with no phages or phage–AuNR under the same conditions).

Temperature Measurement of Cells Using BCECF. To measure the temperature of suspended cells during thermolysis, *E. coli* ER2738 cells attached to the M13KE–AuNR bioconjugates (prepared as described above) were incubated with 10 μ M BCECF solution at room temperature for 20 min. The free dye was removed by centrifugation. The cells were washed three times and resuspended in PBS buffer (0.1 M, pH 7.4). The bulk fluorescence of BCECF ($\lambda_{ex} = 490$ nm, $\lambda_{em} = 500$ to 600 nm) in the sample at room temperature was determined using a Fluoromax-4 spectrofluorometer (Horiba). The presence of AuNRs did not affect the observed spectrum of BCECF (SI Appendix, Fig. S9E). A standard solution of BCECF (0.15 μ M in PBS buffer) was prepared to match the observed bulk fluorescence at room temperature. The fluorescence spectrum of the standard BCECF solution was measured at varying temperatures using a Peltier-based cuvette holder (Horiba) to construct a standard curve. The fluorescence of the *E. coli*–phage–AuNR suspension was recorded simultaneously with laser irradiation from above the sample to induce thermolysis.

To estimate the temperature of cells in a biofilm during thermolysis, a calibration curve was first obtained by recording fluorescence images of a biofilm stained with BCECF at different temperatures (from 25 to 90 °C) using a Lauda Eco RE415 Silver cooling thermostat system (LAUDA-Brinkmann) with a confocal microscope (excitation at 488 nm; TCS SP8; Leica Microsystems). The fluorescence intensities were calculated using ImageJ to obtain the calibration curve between intensity vs. temperature. Cells were identified from background by thresholding and intensities recorded from the "Analyze Particles" tool in ImageJ. Threshold settings were kept identical between images. Between measurements, the microscope laser was shut down, and the sample was covered with aluminum foil to reduce photo-bleaching while the temperature was adjusted. A *P. aeruginosa* biofilm was incubated with M13-g3p(Pf1)–AuNR bioconjugates and stained by BCECF as described above. The free dye was removed by pipetting off the liquid phase and washing three times with PBS buffer. The biofilm was irradiated by NIR light for 10 min as described above, and a fluorescence image was taken immediately.

Viscosity of Cell Membranes Measured by Molecular Rotor BODIPY C10. The viscosity of mammalian and bacterial cell membranes during thermolysis was measured by staining the biofilm with BODIPY C10 (incubation with 10 μ M BODIPY C10 at 37 °C for 20 min followed by replacement of DMEM) and measuring by FLIM before and after NIR laser irradiation (described above). Fluorescence lifetime images were recorded using a time-correlated single-photon counting card (Leica Falcon FLIM). Imaging was achieved using a confocal microscope (TCS SP8; Leica Microsystems) with a Leica SuperK white light laser, which provided pulsed excitation permitting time-resolved fluorescence imaging. The excitation wavelength used was 488 nm. The data were analyzed by LAS X FLIM/FCS software (Leica Falcon FLIM). The bacteria were identified manually by morphology of the cells in confocal microscope images. The viscosities were calculated from FLIM data according to the following viscosity-lifetime calibration

equation, which was obtained by measuring the fluorescence lifetime of BODIPY C10 in different solutions of methanol/glycerol mixtures with known viscosities (43):

$$\log V = \frac{\log T + 0.75614}{0.4569} \quad [1]$$

Here, V is viscosity (in centipoises), and T is fluorescence lifetime (in nanoseconds).

Concentration of AuNRs. Single-particle ICP-MS was performed with an Agilent 7900 ICP-MS (Santa Clara) to determine the concentration of the AuNRs. The phage–AuNR bioconjugates were incubated with 5% nitric acid for a week to degrade the virus before the measurement. The analysis was carried out in a time-resolved analysis mode with an integration time of 100 μ s per point and no settling time between measurements. The data analysis was conducted with the Agilent ICP-MS MassHunter software (version C.01.04 Build 544.3) via single-nanoparticle application module.

TEM. TEM was performed on a Tecnai FEI G2 Sphera microscope (Materials Research Laboratory [MRL], University of California, Santa Barbara) as previously described (31). M13KE–AuNR samples were prepared as described above (*Methods, Visualization of Binding of M13KE–AuNR to E. coli*). The AuNR size was calculated by measuring 200 AuNRs.

Zeta Potential Measurements. Zeta potentials were measured by using a Malvern Zetasizer Nano ZSP operating a 4 mW He–Ne laser at 633 nm as

previously described (31). Data from three or more individual samples were averaged, and each sample was measured five times (10 runs each).

See *SI Appendix, Methods* for description of additional optical characterization, synthesis of AuNRs, colocalization analysis, antibody–AuNR experiments, chimeric phages, phage and bacterial propagation, and EPS quantitation.

Data Availability. All data are included in the manuscript and *SI Appendix*.

ACKNOWLEDGMENTS. Financial support from the NIH (DP2 GM123457-01 to I.A.C.), the Institute for Collaborative Biotechnologies (Contract W911NF-09-0001 from the US Army Research Office), and the National Science Foundation (CMMI 1662431 to B.L.P.) is acknowledged. We thank M. Mahan for bacterial strains and advice, W. J. Nelson for the MDCKII cell line, and Petra Levin for advice on bacterial biofilms. We thank M. Kuimova for kind provision of molecular rotor BODIPY-C10. We acknowledge the use of the Neuroscience Research Institute–Department of Molecular, Cellular, and Developmental Biology Microscopy Facility and the resonant scanning confocal microscope supported by the NSF Major Research Instrumentation Grant DBI-1625770; the Biological Nanostructures Laboratory (UV-vis) within the California NanoSystems Institute, supported by the University of California, Santa Barbara, and the University of California, Office of the President; ICP-MS instrumentation from the Keller Laboratory at University of California, Santa Barbara; and the MRL Shared Experimental Facilities (attenuated total reflection–FTIR, TEM, XPS) supported by the Materials Research Science and Engineering Center Program of the NSF under Award DMR 1720256, a member of the NSF-funded Materials Research Facilities Network (<https://www.mrfn.org>).

- C. Dye, After 2015: Infectious diseases in a new era of health and development. *Philos. Trans. R. Soc. Lond. B Biol. Sci.* **369**, 20130426 (2014).
- R. T. Schooley *et al.*, Development and use of personalized bacteriophage-based therapeutic cocktails to treat a patient with a disseminated resistant *Acinetobacter baumannii* infection. *Antimicrob. Agents Chemother.* **61**, e00954-17 (2017).
- R. M. Dedrick *et al.*, Engineered bacteriophages for treatment of a patient with a disseminated drug-resistant *Mycobacterium abscessus*. *Nat. Med.* **25**, 730–733 (2019).
- K. E. Kortright, B. K. Chan, J. L. Koff, P. E. Turner, Phage therapy: A renewed approach to combat antibiotic-resistant bacteria. *Cell Host Microbe* **25**, 219–232 (2019).
- J. R. Penadés, J. Chen, N. Quiles-Puchalt, N. Carpena, R. P. Novick, Bacteriophage-mediated spread of bacterial virulence genes. *Curr. Opin. Microbiol.* **23**, 171–178 (2015).
- R. J. Citorik, M. Mimee, T. K. Lu, Sequence-specific antimicrobials using efficiently delivered RNA-guided nucleases. *Nat. Biotechnol.* **32**, 1141–1145 (2014).
- D. Bikard *et al.*, Exploiting CRISPR-Cas nucleases to produce sequence-specific antimicrobials. *Nat. Biotechnol.* **32**, 1146–1150 (2014).
- D. P. Pires, S. Cleto, S. Sillankorva, J. Azeredo, T. K. Lu, Genetically engineered phages: A review of advances over the last decade. *Microbiol. Mol. Biol. Rev.* **80**, 523–543 (2016).
- S. Hesse, S. Adhya, Phage therapy in the twenty-first century: Facing the decline of the antibiotic era; is it finally time for the age of the phage? *Annu. Rev. Microbiol.* **73**, 155–174 (2019).
- S. T. Abedon, S. J. Kuhl, B. G. Blasdel, E. M. Kutter, Phage treatment of human infections. *Bacteriophage* **1**, 66–85 (2011).
- B. O. Kim *et al.*, Phage-derived antibacterials: Harnessing the simplicity, plasticity, and diversity of phages. *Viruses* **11**, E268 (2019).
- A. Lin *et al.*, Inhibition of bacterial conjugation by phage M13 and its protein g3p: Quantitative analysis and model. *PLoS One* **6**, e19991 (2011).
- C. Baptista, M. A. Santos, C. São-José, Phage SPP1 reversible adsorption to *Bacillus subtilis* cell wall teichoic acids accelerates virus recognition of membrane receptor YueB. *J. Bacteriol.* **190**, 4989–4996 (2008).
- M. Youle, *Thinking Like a Phage: The Genius of Viruses That Infect Bacteria and Archaea* (Wholon, San Diego, 2017).
- J. J. Barr *et al.*, Subdiffusive motion of bacteriophage in mucosal surfaces increases the frequency of bacterial encounters. *Proc. Natl. Acad. Sci. U.S.A.* **112**, 13675–13680 (2015).
- E. Rothenberg *et al.*, Single-virus tracking reveals a spatial receptor-dependent search mechanism. *Biophys. J.* **100**, 2875–2882 (2011).
- L. Hu *et al.*, Photothermal-responsive single-walled carbon nanotube-based ultrathin membranes for on/off switchable separation of oil-in-water nanoemulsions. *ACS Nano* **9**, 4835–4842 (2015).
- T. Murakami *et al.*, Photodynamic and photothermal effects of semiconducting and metallic-enriched single-walled carbon nanotubes. *J. Am. Chem. Soc.* **134**, 17862–17865 (2012).
- D. K. Lim *et al.*, Enhanced photothermal effect of plasmonic nanoparticles coated with reduced graphene oxide. *Nano Lett.* **13**, 4075–4079 (2013).
- M. Li, X. Yang, J. Ren, K. Qu, X. Qu, Using graphene oxide high near-infrared absorbance for photothermal treatment of Alzheimer’s disease. *Adv. Mater.* **24**, 1722–1728 (2012).
- M. R. K. Ali *et al.*, Targeting cancer cell integrins using gold nanorods in photothermal therapy inhibits migration through affecting cytoskeletal proteins. *Proc. Natl. Acad. Sci. U.S.A.* **114**, E5655–E5663 (2017).
- D. Andrén *et al.*, Probing photothermal effects on optically trapped gold nanorods by simultaneous plasmon spectroscopy and brownian dynamics analysis. *ACS Nano* **11**, 10053–10061 (2017).
- S. Baral, A. Rafiei Miandashti, H. H. Richardson, Near-field thermal imaging of optically excited gold nanostructures: Scaling principles for collective heating with heat dissipation into the surrounding medium. *Nanoscale* **10**, 941–948 (2018).
- P. Rodríguez-Sevilla *et al.*, Thermal scanning at the cellular level by an optically trapped upconverting fluorescent particle. *Adv. Mater.* **28**, 2421–2426 (2016).
- M. Bottagisio, A. B. Lovati, F. Galbusera, L. Drago, G. Banfi, A precautionary approach to guide the use of transition metal-based nanotechnology to prevent orthopedic infections. *Materials* **12**, E314 (2019).
- R. S. Norman, J. W. Stone, A. Gole, C. J. Murphy, T. L. Sabo-Attwood, Targeted photothermal lysis of the pathogenic bacteria, *Pseudomonas aeruginosa*, with gold nanorods. *Nano Lett.* **8**, 302–306 (2008).
- J. Yu *et al.*, Improved anticancer photothermal therapy using the bystander effect enhanced by antiarrhythmic peptide conjugated dopamine-modified reduced graphene oxide nanocomposite. *Adv. Healthc. Mater.* **6**, 1600804 (2017).
- K. Yang *et al.*, Graphene in mice: Ultrahigh in vivo tumor uptake and efficient photothermal therapy. *Nano Lett.* **10**, 3318–3323 (2010).
- L. Yang *et al.*, Photothermal therapeutic response of cancer cells to aptamer-gold nanoparticle-hybridized graphene oxide under NIR illumination. *ACS Appl. Mater. Interfaces* **7**, 5097–5106 (2015).
- P. Chakravarty *et al.*, Thermal ablation of tumor cells with antibody-functionalized single-walled carbon nanotubes. *Proc. Natl. Acad. Sci. U.S.A.* **105**, 8697–8702 (2008).
- H. Peng, I. A. Chen, Rapid colorimetric detection of bacterial species through the capture of gold nanoparticles by chimeric phages. *ACS Nano* **13**, 1244–1252 (2019).
- B. L. Hurwitz, M. B. Sullivan, The Pacific Ocean virome (POV): A marine viral metagenomic dataset and associated protein clusters for quantitative viral ecology. *PLoS One* **8**, e57355 (2013).
- B. Koskella, S. Meaden, Understanding bacteriophage specificity in natural microbial communities. *Viruses* **5**, 806–823 (2013).
- X. Ye *et al.*, Improved size-tunable synthesis of monodisperse gold nanorods through the use of aromatic additives. *ACS Nano* **6**, 2804–2817 (2012).
- S. Jayabal *et al.*, A gold nanorod-based localized surface plasmon resonance platform for the detection of environmentally toxic metal ions. *Analyst (Lond.)* **140**, 2540–2555 (2015).
- X. Xia *et al.*, Quantifying the coverage density of poly(ethylene glycol) chains on the surface of gold nanostructures. *ACS Nano* **6**, 512–522 (2012).
- E. Pensa *et al.*, The chemistry of the sulfur-gold interface: In search of a unified model. *Acc. Chem. Res.* **45**, 1183–1192 (2012).
- B. Reiser, L. González-García, I. Kanelidis, J. H. M. Maurer, T. Kraus, Gold nanorods with conjugated polymer ligands: Sintering-free conductive inks for printed electronics. *Chem. Sci. (Camb.)* **7**, 4190–4196 (2016).
- Z. Zhang, M. S. Lin, Fast loading of PEG-SH on CTAB-protected gold nanorods. *RSC Adv* **4**, 17760–17767 (2014).
- M. R. K. Ali *et al.*, Efficacy, long-term toxicity, and mechanistic studies of gold nanorods photothermal therapy of cancer in xenograft mice. *Proc. Natl. Acad. Sci. U.S.A.* **114**, E3110–E3118 (2017).
- G. A. O’Toole, Microtiter dish biofilm formation assay. *J. Vis. Exp.* **47**, e2437 (2011).
- J. D. Dukes, P. Whitley, A. D. Chalmers, The MDCK variety pack: Choosing the right strain. *BMC Cell Biol.* **12**, 43 (2011).

43. J. T. Mika *et al.*, Measuring the viscosity of the *Escherichia coli* plasma membrane using molecular rotors. *Biophys. J.* **111**, 1528–1540 (2016).
44. B. Byrne, E. Stack, N. Gilmartin, R. O’Kennedy, Antibody-based sensors: Principles, problems and potential for detection of pathogens and associated toxins. *Sensors (Basel)* **9**, 4407–4445 (2009).
45. B. K. Hahm, A. K. Bhunia, Effect of environmental stresses on antibody-based detection of *Escherichia coli* O157:H7, *Salmonella enterica* serotype Enteritidis and *Listeria monocytogenes*. *J. Appl. Microbiol.* **100**, 1017–1027 (2006).
46. S. Hearty, P. Leonard, J. Quinn, R. O’Kennedy, Production, characterisation and potential application of a novel monoclonal antibody for rapid identification of virulent *Listeria monocytogenes*. *J. Microbiol. Methods* **66**, 294–312 (2006).
47. L. S. Frost, J. S. Lee, D. G. Scraba, W. Paranchych, Two monoclonal antibodies specific for different epitopes within the amino-terminal region of F pilin. *J. Bacteriol.* **168**, 192–198 (1986).
48. J. P. Landry, Y. Ke, G. L. Yu, X. D. Zhu, Measuring affinity constants of 1450 monoclonal antibodies to peptide targets with a microarray-based label-free assay platform. *J. Immunol. Methods* **417**, 86–96 (2015).
49. Y. Wine *et al.*, Molecular deconvolution of the monoclonal antibodies that comprise the polyclonal serum response. *Proc. Natl. Acad. Sci. U.S.A.* **110**, 2993–2998 (2013).
50. S.-H. Jung, C.-M. Ryu, J.-S. Kim, Bacterial persistence: Fundamentals and clinical importance. *J. Microbiol.* **57**, 829–835 (2019).
51. L. Van Valen, A new evolutionary law. *Evol. Theory* **1**, 1–30 (1973).
52. R. Serra *et al.*, Chronic wound infections: The role of *Pseudomonas aeruginosa* and *Staphylococcus aureus*. *Expert Rev. Anti Infect. Ther.* **13**, 605–613 (2015).
53. K. H. Turner, J. Everett, U. Trivedi, K. P. Rumbaugh, M. Whiteley, Requirements for *Pseudomonas aeruginosa* acute burn and chronic surgical wound infection. *PLoS Genet.* **10**, e1004518 (2014).
54. D. Lebeaux, J. M. Ghigo, C. Beloin, Biofilm-related infections: Bridging the gap between clinical management and fundamental aspects of recalcitrance toward antibiotics. *Microbiol. Mol. Biol. Rev.* **78**, 510–543 (2014).
55. E. Tacconelli, N. Magrini, “Global priority list of antibiotic-resistant bacteria to guide research, discovery, and development of new antibiotics” (World Health Organization, 2017).
56. D. L. Kernan, A. M. Wen, A. S. Pitek, N. F. Steinmetz, Featured article: Delivery of chemotherapeutic vcMMAE using tobacco mosaic virus nanoparticles. *Exp. Biol. Med. (Maywood)* **242**, 1405–1411 (2017).
57. D. A. Marvin, B. Hohn, Filamentous bacterial viruses. *Bacteriol. Rev.* **33**, 172–209 (1969).
58. M. Clarke, L. Maddera, R. L. Harris, P. M. Silverman, F-pili dynamics by live-cell imaging. *Proc. Natl. Acad. Sci. U.S.A.* **105**, 17978–17981 (2008).